This document is the accepted manuscript version of the following article:
Tang, L., Watts, B., Thomsen, L., & McNeill, C. R. (2021). Morphology and charge transport properties of P(NDI2OD-T2)/polystyrene blends. Macromolecules, 54(23), 11134-11146. https://doi.org/10.1021/acs.macromol.1c01661

Morphology and charge transport properties of P(NDI2OD-T2)/polystyrene blends

Linjing Tang,[a] *Benjamin Watts,*[b] *Lars Thomsen*[c] *and Christopher R. McNeill*[a*]

[a] Department of Materials Science and Engineering, Monash University, Wellington Road, Clayton, Victoria 3800, Australia

[b] Swiss Light Source, Paul Scherrer Institut, Villigen-PSI, CH-5232, Switzerland

[c] Australian Synchrotron, ANSTO, 800 Blackburn Road, Clayton, Victoria 3168, Australia

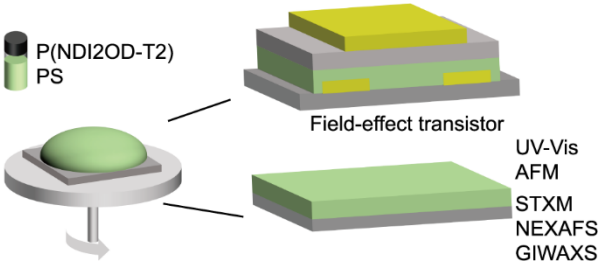

For Table of Contents Only

Abstract

While the strategy of blending commodity insulating polymers with conjugated polymers has been previously applied to modify the properties of organic field-effect transistors (OFETs), comprehensive studies on the evolution of morphology and OFET performance with film composition are scarce. In this contribution, films comprising the n-type semiconducting polymer P(NDI2OD-T2) and the insulating polymer polystyrene (PS) were explored in detail. In particular, the electrical properties and film

morphology of blends with a P(NDI2OD-T2) concentration ranging from 0.125 wt.% to 100 wt.% were studied. Two regimes characterized by distinct dependencies of device mobility as a function of P(NDI2OD-T2) content were observed: Above 12.5 wt.% P(NDI2OD-T2), the OFET mobility showed a weak dependence on P(NDI2OD-T2) concentration despite the presence of strong lateral phase separation, while below 12.5% the device mobility was observed to decrease strongly with decreasing P(NDI2OD-T2) concentration attributed to disrupted surface connectivity of the P(NDI2OD-T2) phase. UV-Vis absorption spectroscopy and grazing incidence wide-angle X-ray scattering (GIWAXS) measurements indicate that the aggregation and crystalline packing are not strongly affected by the presence of PS. Atomic force microscopy (AFM) and scanning transmission X-ray spectro-microscopy (STXM) reveal lateral phase separation for blends with compositions of 87.5 wt.% to 25 wt.% P(NDI2OD-T2). Enrichment of P(NDI2OD-T2) at the film surface is confirmed by near-edge X-ray absorption fine structure (NEXAFS) spectroscopy, with a high P(NDI2OD-T2) surface composition (> 80 wt.%) maintained down to an overall blend composition of 12.5 wt.% P(NDI2OD-T2). The strong decrease in OFET mobility for P(NDI2OD-T2) concentration less than 25 wt.% is attributed to a loss of P(NDI2OD-T2) surface connectivity at low P(NDI2OD-T2) loading. We also observe a transition from face-on to edge-on dominated configuration at low P(NDI2OD-T2) content with GIWAXS, consistent with an edge-on surface layer that persists down to monolayer surface coverage.

Introduction

Over the past several decades, organic semiconductors have been extensively researched as an alternative to conventional silicon-based semiconductors. Moreover the molecular structure of organic semiconductors can be tailored to provide advantageous material properties. For example, the physical properties of organic semiconductors can be readily tuned by modifying their π-conjugated cores and/or side chains. As a consequence, most organic semiconductors can be processed from solution at room temperature, permitting high-throughput and large-scale manufacture at low cost.[1] Among the variety of

organic semiconductors developed so far, poly(3-hexylthiophene) (P3HT) and poly{[N,N-9-bis(2-octyldodecyl) naphthalene-1,4,5,8-bis(dicarboximide)-2,6-diyl]-alt-5,59-(2,29-bithiophene)} (P(NDI2OD-T2)) can be considered as two key representative semiconducting polymers having been extensively studied as platforms to establish processing-morphology-property relationships to provide guidelines for producing high-performance organic electronics.[2-11] A method that allows a convenient way to control film morphology is to blend semiconducting polymers with commodity insulating polymers such as polystyrene (PS) or poly(methyl methacrylate) (PMMA). Numerous studies applying this method to P3HT have been reported.[12-20] For example, by mixing P3HT with PS in dichloromethane, Qiu et al. obtained a network of highly crystalline P3HT nanofibers and achieved a comparable hole mobility to that of neat P3HT even for a P3HT content down to 5 wt.%.[21] Apart from improving electrical properties, this strategy can also be used to improve the mechanical properties: polymeric semiconductors can be quite brittle so blending with commodity polymers can improve mechanical flexibility with a view towards wearable organic electronics. For example, Zhang et al. achieved enhanced visual transparency and mechanical elasticity even under 100% strain with P3HT/PDMS (polydimethylsiloxane) blend films containing only a small proportion of P3HT.[12]

Since being first reported by Chen et al. in 2008, many in-depth microstructural and morphological studies have been performed on P(NDI2OD-T2).[2-5, 7, 8, 22-30] Polymer chain aggregation and thin film crystallinity are the properties that are generally of most interest. Owing to its donor-acceptor nature, the UV-Vis absorption spectrum of P(NDI2OD-T2) possesses two absorption bands: one centered at ~400 nm ascribed to the π-π* transition and a lower energy absorption band between 600 nm to 800 nm ascribed to the charge transport transition (CT band).[3, 5, 25, 26, 30, 31] With its high sensitivity to chain conformation, the spectral profile of the CT absorption is frequently used to study polymer aggregation behavior.[5, 25, 26, 30] GIWAXS measurements of P(NDI2OD-T2) thin films generally find a dominant face-on orientation of crystallites in the bulk of as-cast films and in films annealed below the melting temperature.[7, 28, 29] However, surface-sensitive angle-resolved NEXAFS spectroscopy has been used to

evidence a distinct edge-on configuration at the surface in contrast to the face-on texture in the bulk.[29] Like many conjugated polymers, P(NDI2OD-T2) chains tend to form elongated structures in the film state, which can be enhanced via the pre-formation of rod-like aggregates in marginal solvents or by recrystallizing from the melting state.[27, 28] To control P(NDI2OD-T2) film morphologies for high-performance organic field effect transistors (OFETs), various methods have been widely explored such as thermal annealing and meniscus-guided coating.[3, 4, 32] Yet, unlike P3HT, the method of blending P(NDI2OD-T2) with insulating polymers has been rarely applied.[31, 33-36] Summarizing prior work, Wang et al. were the first to report on P(NDI2OD-T2)/PS blends for OFET applications, showing that the face-on orientation is unaffected in the bulk and arguing that long-range order in the P(NDI2OD-T2) is not as significant as previously thought for high mobility in OFETs. Characteristic fibrillar features were preserved in blends with PS down to 1 wt.% P(NDI2OD-T2).[35] Angunawela et al.[33] also observed comparable charge carrier mobilities in OFET devices made using P(NDI2OD-T2)/PS blends compared to those utilizing neat P(NDI2OD-T2) films, and found that the elongated features of P(NDI2OD-T2) were preserved in P(NDI2OD-T2)/PS blends, corroborating the study of Wang et al.[35] In addition to PS, polyacrylonitrile (PAN) and other insulating polymers have been blended with P(NDI2OD-T2). In the study by Dong et al., P(NDI2OD-T2) was blended with PAN which was found to greatly improve air stability.[36] Similarly, P(NDI2OD-T2)/PAN blends were also investigated by Jiang et al. with PAN found to increase the size of P(NDI2OD-T2) aggregates in solution and the size of crystalline grains in thin films as a result.[31] Yang et al. reported blends of P(NDI2OD-T2) with three different polymers: isotactic polypropylene (iPP), atactic polypropylene (aPP) and poly(ethylene oxide) (PEO) in various ratios, and demonstrated that the degree of order along the π-π stacking, lamellar stacking and backbone could be tuned independently. Assuming a linear relationship between the charge mobility and the order degree along π-π stacking and backbone direction, they correlated these three parameters via multivariable linear regression, finding a greater impact of π-π stacking over backbone packing on the charge carrier mobility, in contrast to the prior study of Wang et al. mentioned above.[34]

The fact that blending with an insulating material sometimes results in improved electrical properties of semiconducting polymers and sometimes not speaks to a gap in our knowledge of how insulating materials interact with semiconducting polymers. With this in mind, we have undertaken an extensive investigation of the P(NDI2OD-T2)/PS blend system to gain a deeper understanding of the effect of PS on film morphology and electrical properties. We also place a particular focus on the relationship between lateral and vertical phase separation. Unlike Wang et al.[35] who neglected lateral phase separation – since the only blend ratio they studied which exhibited lateral phase separation did not support charge transport – we find that good OFET performance is maintained in the presence of strong lateral phase separation. Angunawela et al.[33] also neglected lateral phase separation as it was not evident from their AFM images. In contrast to these studies we study the evolution of lateral and vertical phase separation across a full range of compositions with bulk and surface sensitive techniques to map out the interplay between lateral and vertical phase separation. Indeed, a suite of advanced characterization techniques has been employed to study various aspects of film morphology, such as polymer aggregation, lateral phase separation, vertical phase separation and thin film crystallinity. Combining these various characterization techniques, we reveal how film morphology varies with film composition and connect this to the corresponding evolution in charge transport properties, offering a detailed perspective for developing high-performance organic transistors based on blend systems in an efficient and cost-effective manner.

Materials and methods

Materials

P(NDI2OD-T2) (M_n = 64.1 kDa, $Đ$ = 2.07, batch No. N052006001) was purchased from Raynergy Tek. Polystyrene (PS) with M_n of 32.4 kDa and $Đ$ = 1.03 and analytical grade chlorobenzene (CB) were both purchased from Sigma Aldrich and used as received. The fluoropolymer CYTOP-809 was purchased from AGC Chemicals Company and used as received without any dilution. Polyethyleneimine ethoxylate (PEIE) was sourced from Sigma Aldrich and diluted with 2-methoxyethanol to 0.01 wt.%.

Device fabrication and characterization

P(NDI2OD-T2) and PS were separately dissolved in CB at the same concentration of 8 mg/mL and then heated at 80 °C for ~24 hours before mixing. Solutions were blended in such a way to maintain a total polymer concentration of 8 mg/mL but with varied P(NDI2OD-T2) content: 100 wt.%, 87.5 wt.%, 75 wt.%, 62.5 wt.%, 50 wt.%, 37.5 wt.%, 25 wt.%, 12.5 wt.%, 6.25 wt.%, 3.75 wt.%, 1.25 wt.%, 0.625 wt.%, 0.25 wt.% and 0.125 wt.%. Note: when referring to the wt.% of P(NDI2OD-T2), it is the weight percentage of P(NDI2OD-T2) in the solute and not of the solution system as a whole. All blend solutions along with two neat solutions were heated at 80 °C for another 24 hours and then allowed to cool down to room temperature and age for 1 to 3 days to reach a thermodynamically stable state.

The top-gate bottom-contact (TGBC) configuration was employed for OFET devices fabricated in the present study. Patterning of source and drain electrodes was achieved via conventional photolithography at the Melbourne Center for Nanofabrication (MCN) with fixed channel width of W = 10 mm and channel length of L = 20 μm. These patterned substrates were cleaned sequentially with acetone and isopropanol in an ultrasonic bath for 10 minutes each and then treated with oxygen plasma for another 10 min. Prior to spin-coating of the semiconductor layer, an ultrathin PEIE layer was formed by spin coating a 2-methoxyethanol solution to facilitate electron injection and block hole injection.[37] After baking the PEIE-coated substrates at 100 °C for 10 min to remove residual solvent, the active semiconducting layer was formed via spin coating from the pre-prepared blend solutions. The semiconducting layer was then thermally annealed at 180 °C on a hotplate in a nitrogen-filled glovebox for 20 min followed by rapid quenching to room temperature by placing on a metal plate. The fluoropolymer CYTOP (relative permittivity k ~2.0) was used as the dielectric layer and deposited by spin coating at 9000 rpm for 2 min, generating a 500 nm thick film (C_i = 3.7 nF/cm^2). The CYTOP layer was then baked under a nitrogen atmosphere at 110 °C for 1 hour to completely remove any residual solvent. Finally, 50 nm of Al was thermally deposited under high vacuum at a constant rate of 1 Å/s as the gate electrode. Unless specified, the whole fabrication process was accomplished in ambient environment. Current-voltage (I-V) characteristics of the OFETs were measured with an Agilent B2902A 2-channel source-measure unit in

conjunction with a Signatone H150 probe station housed inside a nitrogen-filled glovebox. Charge carrier mobility (μ) and threshold voltage (V_T) were extracted according to the equation below in the saturation regime of the transfer curves, where W and L are the channel width and channel length, respectively.

$$\sqrt{I_D}=\sqrt{\frac{\mu W C_i}{2L}}(V_G - V_T) \quad (1)$$

UV–Vis absorption spectroscopy

UV–Vis absorption measurements were acquired using a PerkinElmer Lambda 950 spectrometer. Samples for these experiments were spin-coated onto glass slides from the same solutions used for device fabrication. Glass substrates were also coated with a PEIE layer before depositing the semiconducting layer to match device fabrication.

Atomic force microscopy (AFM)

AFM measurements were performed on a Bruker Dimension Icon AFM using ScanAsyst mode at the MCN. Films were coated onto Si/SiO_2 substrates. Before spin-coating of the semiconductor layer, a PEIE layer was cast onto the substrates to match the condition of device fabrication. AFM data were processed using Gwyddion.

Scanning transmission X-ray spectro-microscopy (STXM)

STXM measurements were conducted at the Swiss Light Source in Switzerland.[38] STXM samples were prepared following the same route as in device fabrication except that a water-soluble sodium polystyrene sulfonate (NaPSS) layer was deposited prior to coating the semiconducting layer. Subsequently, semiconducting films were delaminated by floating off in deionized water and then transferred to the supporting TEM grids. Details about the measurement parameters can be found in the supplementary information (Figure S1). In particular, appropriate dwell times were chosen to mitigate the effects of beam damage. STXM data were processed using the IDL widget aXis2000. Further details regarding the principles of STXM and methodology for extracting quantitative chemical maps can be found elsewhere.[39]

Grazing incidence wide-angle X-ray scattering (GIWAXS)

GIWAXS measurements were performed on the SAXS/WAXS beamline at the Australian Synchrotron.[40] Samples for GIWAXS measurements were cast onto bare Si substrates under the same processing conditions as for OFET fabrication. X-rays with an energy of 15 keV (0.827 nm) were directed onto the samples using a series of incident angles ranging from 0.07° to 0.12°. Exposure time was set to 1 s, with 3 × 1 s exposures taken at different lateral offsets of the detector to fill in the gaps between module elements, with these three exposures stitched in software. Measurement for each incident angle was recorded at a fresh spot to avoid beam damage. Scattering patterns were collected on a two-dimensional Dectris Pilatus 2 M detector with pixel size of 0.172 mm × 0.172 mm placed 696 mm downstream from the sample stage. Samples were measured under vacuum, with the entire beam path being contained in vacuum to minimize air scatter. GIWAXS data were processed using a modified version of the Nika package implemented within IgorPro.[41] Peak locations and widths were extracted via peak fitting with further details provided in Table S1.

Near-edge X-ray absorption fine structure (NEXAFS) spectroscopy

NEXAFS spectroscopy measurements were conducted at the Soft X-ray beamline at the Australian Synchrotron.[42] Bare, highly doped Si substrates were used to support sample films to facilitate total electron mode (TEY) collection. The incident angle was fixed at the magical angle of 55° to negate orientation effects. TEY collection was performed by measuring the drain current flowing to the sample, while partial electron yield (PEY) collection was acquired with a channeltron detector by measuring photoelectrons emitted from the sample with kinetic energy above a certain threshold determined by the retarding voltage of 250 V. TEY and PEY have different sampling depths, both showing high surface sensitivity with TEY probing deeper than PEY for a given condition. Probing depth varies from case to case from 1 nm – 10 nm.[29, 43-45] Data were analyzed using QANT implemented in IgorPro.[46] Chemical composition of the surface of blend films was determined by fitting blend spectra with a linear combination of reference neat spectra. Further details can be found elsewhere.[47]

Results and discussion

Optical properties. Figure 1 displays the UV–Vis absorption spectra of films with varying P(NDI2OD-T2) content. Films with > 3.75 wt.% P(NDI2OD-T2) all show discernable P(NDI2OD-T2) absorption features with characteristic peaks at 400 nm and 710 nm, with a longer wavelength shoulder at around 800 nm (Figure 1a and Figure 1b). The absorption at 400 nm arises due to π-π* transitions, while absorption in the range of 600 nm to 800 nm arises due to charge transfer or CT transitions. For films with P(NDI2OD-T2) less than 3.75 wt.%, clear P(NDI2OD-T2) absorption features could not be seen due to the limited amount of P(NDI2OD-T2) combined with a strong scattering background. Variation in the shape of the CT absorption features is indicative of the state of polymer aggregates.[4, 22, 27, 30] Therefore normalizing spectra in Figure 1 allows us to compare the aggregate state across all films, as presented in Figure S2. Overall, no significant difference is discernable in the shape of the absorption spectra, pointing to a similar aggregation state independent of the P(NDI2OD-T2) content. To explain the aggregation behavior in even highly diluted P(NDI2OD-T2) films, it is postulated that P(NDI2OD-T2) chains aggregate during spin coating. In other words, P(NDI2OD-T2) chains are not homogenously distributed within the film but phase-segregated from PS, which is verified by AFM, STXM and NEXAFS measurements as shall be detailed in the following sections.

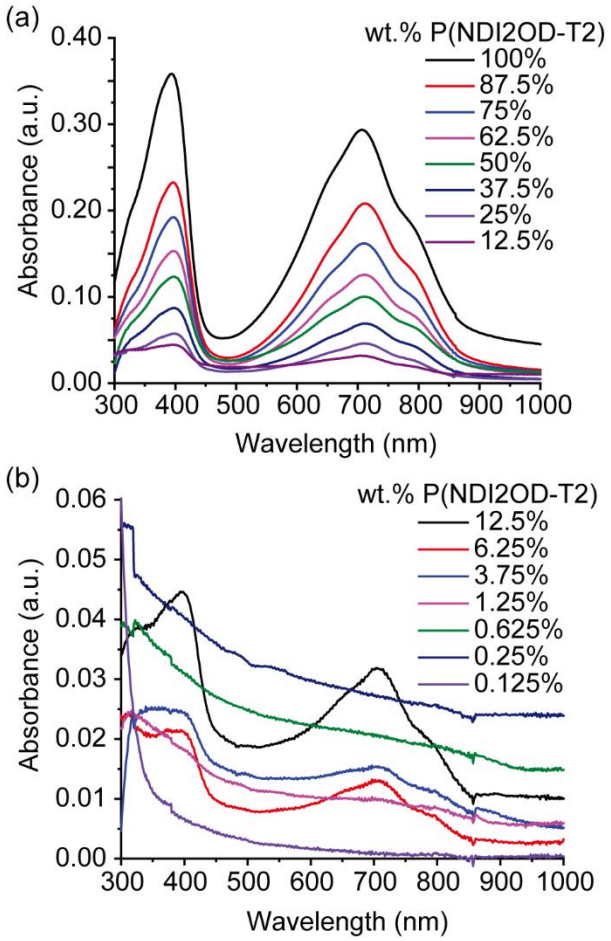

Figure 1. UV–Vis absorption spectra of films containing various P(NDI2OD-T2) content. For clarity, curves are separately plotted in two graphs.

Surface topography. AFM height images for blend films with different P(NDI2OD-T2) content are displayed in Figure 2. The AFM image of the neat P(NDI2OD-T2) film shows characteristic elongated fibrils (Figure 2a), consistent with previous studies.[5, 23-25, 27, 33, 35] Figure S3 shows typical height profiles taken from the AFM images of pristine P(NDI2OD-T2) film from which the width and height of fibrils are of size ~300 nm and ~5 nm respectively. Upon incorporation of PS, lateral phase separation is observed in the AFM images for samples with P(NDI2OD-T2) ranging from 25 wt.% to 87.5 wt.%. The continuous phase appears to be covered by fibrils that are characteristic of P(NDI2OD-T2) and so is likely to be P(NDI2OD-T2)-rich. The enclosed domains have a smoother surface and are likely to correspond to PS-rich domains. Chemical mappings of some of these blend films constructed from

STXM data verify these presumptions (discussed later). Samples with 12.5 wt.% P(NDI2OD-T2) and lower exhibit a smooth, apparently homogenous topography reflecting the absence of lateral phase separation. We note that our AFM results are different to the reports of Wang et al. and Angunawela et al. who also studied P(NDI2OD-T2) blended with PS.[33, 35] Angunawela et al. reported a lack of phase separation and inferred a high degree of miscibility, reflected by various characterization tools.[33] Wang et al.[35] observed lateral phase separation in their 40% P(NDI2OD-T2) sample but did not extensively study lateral phase separation as it was associated with poor OFET performance. Differences in the observed morphologies are likely to be influenced by the molar masses used. Angunawela et al. used relatively low molar mass batches of P(NDI2OD-T2) (M_n = 9 kDa) and PS (2 kDa) which could help to explained the high degree of miscibility.[33] In both the present study and that of Wang et al.[35] where lateral phase separation is observed, higher molar masses of P(NDI2OD-T2) and/or PS were used. In the present study molar masses of M_n = 64 kDa and M_n = 32 kDa were used for P(NDI2OD-T2) and PS, respectively, while a molar mass of 100 kDa for PS was used in the work of Wang et al.[35] (the molar mass of P(NDI2OD-T2) was not specified). To confirm a strong influence of molar mass on morphology, we have performed AFM measurements on films of P(NDI2OD-T2) blended with PS with molar masses of ~35 kDa, ~200 kDa and ~2000 kDa for a weight ratio of 1:1, as shown in Figure S4. The AFM images of these samples show remarkably distinct morphologies with a higher degree of phase separation and RMS roughness when a higher molar mass of PS is used. It is expected that the molar mass of P(NDI2OD-T2) will also play a role.[5] Differences in the solution preparation protocols used are also likely to influence the resulting morphology. 1,2-dichlorobenzene was used as the solvent in the studies of Wang et al. and Angunawela et al. while chlorobenzene was used in the present work, with P(NDI2OD-T2) known to have a higher degree of aggregation in 1,2-dichlorobenzene than chlorobenzene.[27, 30] Furthermore, in the present study, prior to coating, solutions were aged for 1 – 3 days to promote the aggregation of P(NDI2OD-T2) chains,[48, 49] with solution aging not mentioned in the other two studies. The aging effect on the morphology of P(NDI2OD-T2) is demonstrated in Figure S5 where

the same solution produced films with different morphologies depending on the solution state; films with larger size domains were generated after the solution was aged for a longer time.

Figure 3 plots the Root Mean Square (RMS) roughness as a function of P(NDI2OD-T2) content. The introduction of PS leads to a significant increase of RMS roughness from 1.3 nm for pristine P(NDI2OD-T2) film to > 5 nm for blend films containing 50 wt.% – 75 wt.% P(NDI2OD-T2). However, for blend films with P(NDI2OD-T2) less than 50 wt.%, the RMS roughness drops with reducing P(NDI2OD-T2) down to 2.3 nm for the film with 25 wt.% P(NDI2OD-T2). In the range of 1.25 wt.% – 12.5 wt.% P(NDI2OD-T2), the RMS roughness becomes very low, < 0.5 nm, comparable to that of pristine PS films, and does not show any marked variation. Overall, films with 25 wt.% – 100 wt.% P(NDI2OD-T2) all show fibrils and RMS roughness over 1 nm, and even over 3 nm for those blend films with a high degree of phase separation (Figure 2b – Figure 2f). However, for films with P(NDI2OD-T2) < 25 wt.%, no fibrils are seen and their surface topography seems to be largely controlled by the PS component. Based on these observations, it is postulated that film roughness is related to the degree of phase separation and the formation of P(NDI2OD-T2) fibrils.

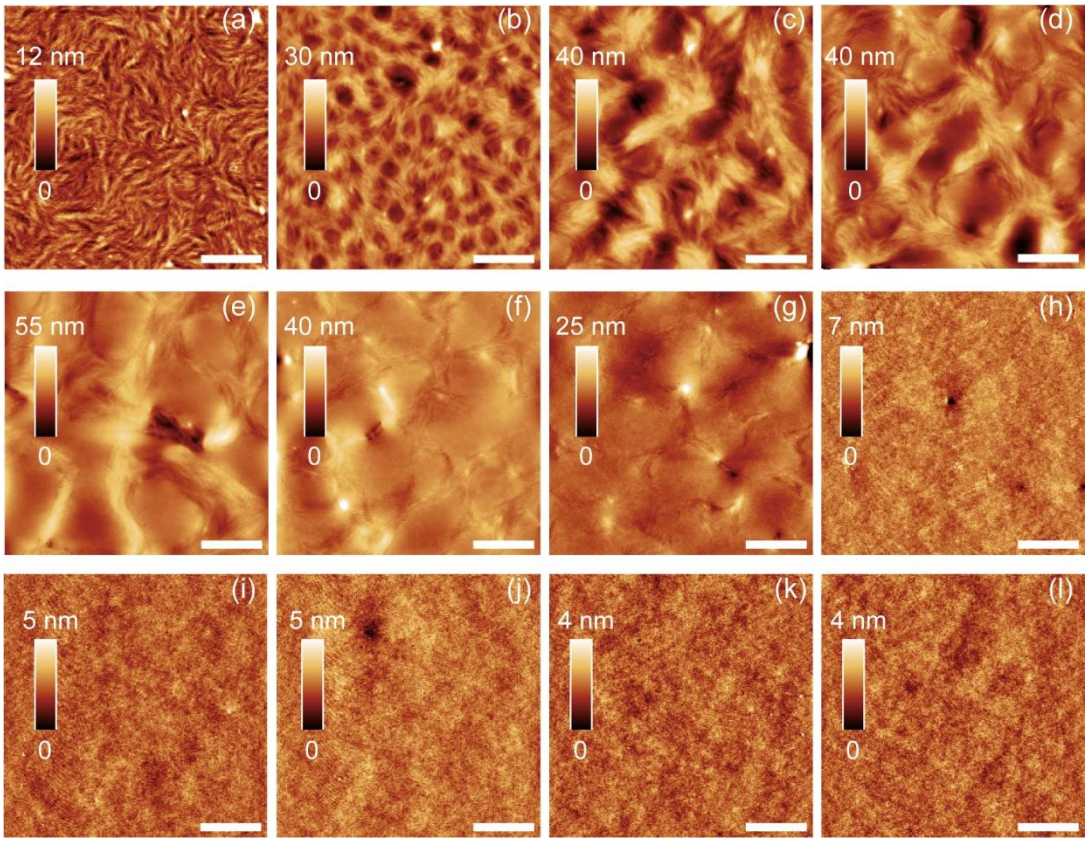

Figure 2. 5 µm × 5 µm AFM height images of films with P(NDI2OD-T2) content of: 100% (a), 87.5% (b), 75% (c), 62.5% (d), 50% (e), 37.5% (f), 25% (g), 12.5% (h), 6.25% (i), 3.75% (j), 1.25% (k) and 0% (l). Scale bars are 1 µm.

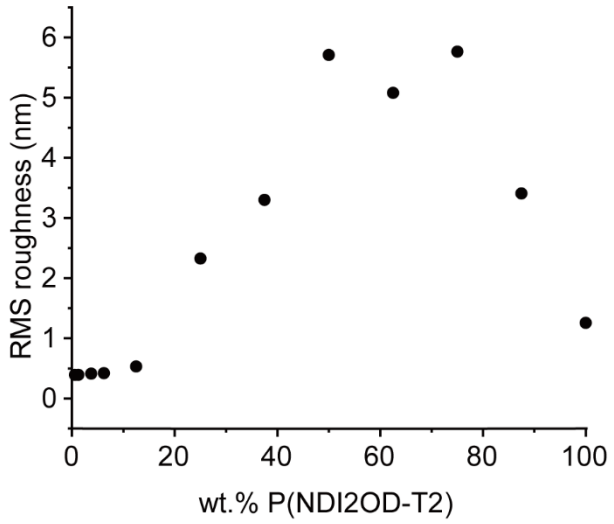

Figure 3. RMS film roughness as a function P(NDI2OD-T2) content.

Lateral phase separation. To unambiguously verify the lateral phase separation observed in the AFM images in Figure 2a – Figure 2g, STXM was used to map the chemical composition in the blend films. Taking advantage of the chemical sensitivity of X-ray absorption near the carbon K-edge along with the capability of Fresnel zone plate to focus X-rays down to a spot size of < 7 nm,[50] STXM can provide a composition map in a high spatial resolution (30.5 nm in the present study).[39] By measuring the X-ray absorption spectrum of neat P(NDI2OD-T2) and neat PS of known thickness, a reference spectrum for each material be attained. For a blend sample where composition varies from point to point, provided STXM images are acquired at multiple judicious energies, the observed X-ray absorption of the blend as a function of X-ray energy and position can be quantitatively deconvoluted to generate a composition map. According to the C K-edge NEXAFS spectra of pure P(NDI2OD-T2) and PS films shown in Figure 4a, X-rays with energies of 283.6 eV, 284.6 eV, 287.25 eV and 288.3 eV were selected for imaging to achieve the best chemical contrast, of which 283.6 eV and 287.25 eV are characteristic of P(NDI2OD-T2) and 284.6 eV and 288.3 eV of PS. Figure 4b – 4d shows the composition maps of films with P(NDI2OD-T2) contents of 75 wt.%, 50 wt.% and 25 wt.% in which the P(NDI2OD-T2) phase is highlighted as the lighter color. Figure S6 displays the corresponding maps where the PS phase is highlighted. In contrast to AFM that probes the film surface, STXM provides a depth-averaged measurement of the composition of the full thickness of the sample. In the film with a high P(NDI2OD-T2) content (Figure 4b), a uniform P(NDI2OD-T2) phase is seen. For a 1:1 P(NDI2OD-T2):PS blend, a high degree of phase separation is observed where P(NDI2OD-T2) and PS form a bi-continuous system (Figure 4c and Figure S6b). When P(NDI2OD-T2) becomes the minority component, its connectivity suffers (Figure 4d) with a poorly connected, elongated phase embedded in the PS matrix (Figure S6c). The trend of P(NDI2OD-T2) distribution within the film shown in Figure 4b – 4d is consistent with the continuous phase found in the AFM images (Figure 2c, e, g), supporting our hypothesis about the domain component in the AFM images, i.e., that the thicker, continuous phase corresponds to P(NDI2OD-T2) and the thinner, enclosed domains with smooth surface correspond to PS.

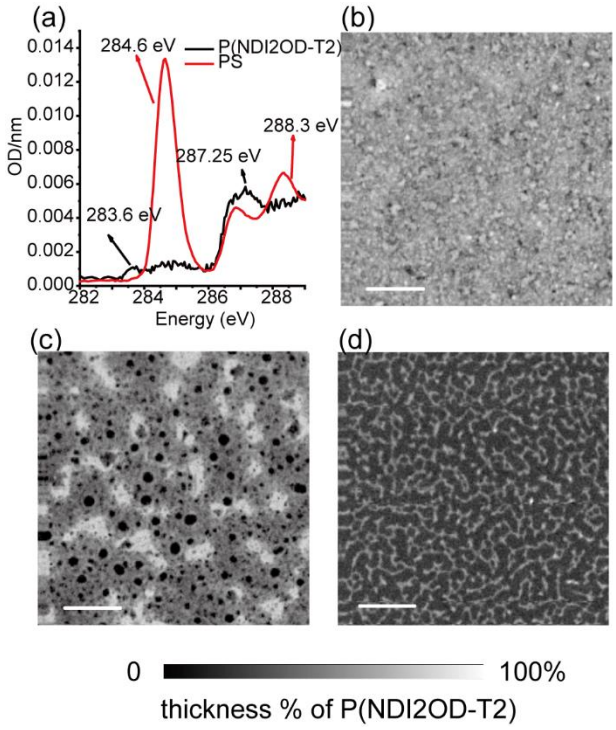

Figure 4. (a) Normalized X-ray absorption spectra of neat P(NDI2OD-T2) and PS films near the C K-edge recorded in transmission mode with characteristic peaks of P(NDI2OD-T2) and PS highlighted. 25 μm × 25 μm STXM composition maps of blend films with 75 wt.% (b), 50 wt.% (c) and 25 wt.% (d) P(NDI2OD-T2). P(NDI2OD-T2) phase is highlighted in lighter color. Scale bars are 5 μm.

Vertical phase separation. During the operation of an OFET, charge transport occurs within a thin layer at the semiconductor/dielectric interface. Therefore, it is essential to probe the interface properties of the semiconducting layer to properly correlate microstructure with OFET operation. Combining surface sensitivity and element sensitivity, NEXAFS spectroscopy can be used to measure chemical composition at the surface of a blend film on the basis that the NEXAFS absorption of a blend film is a simple linear combination of that of individual components. See Figure S7 for the original NEXAFS spectra of those blend films and how the contribution of P(NDI2OD-T2) and PS is derived for each spectrum using *QANT*. Figure 5a plots the surface composition of PEY and TEY modes as a function of P(NDI2OD-T2) content within the whole film. A larger P(NDI2OD-T2) content is consistently measured at the surface compared to the bulk average. Furthermore, a higher P(NDI2OD-T2) surface content is

measured under PEY mode than under TEY mode, suggesting a very thin P(NDI2OD-T2) enriched surface layer. These observations indicate the strong propensity of P(NDI2OD-T2) to segregate at the surface, which is understandable given the lower surface free energy of ~24 $mJ \cdot m^{-2}$ of P(NDI2OD-T2) compared to PS (~40 $mJ \cdot m^{-2}$).[35] Unlike the overall film composition for which the P(NDI2OD-T2) content decreases linearly, the evolution of surface composition probed by NEXAFS can be roughly divided into two regimes differing in changing slope. In the regime where overall P(NDI2OD-T2) content drops from 100 wt.% to 12.5 wt.% (regime I), P(NDI2OD-T2) at the surface remains > 80 wt.% and experiences only a decrease from 100 wt.% to 82 wt.%, suggesting that the film surface is predominately covered by P(NDI2OD-T2). Thus, although AFM and STXM record lateral phase separation, there appears to be a relatively continuous P(NDI2O-T2) capping layer, even for those regions that appear smooth. In contrast, reducing the overall P(NDI2OD-T2) content from 12.5 wt.% to 0.625 wt.% (regime II), the P(NDI2OD-T2) content at the surface is observed to decrease drastically from 82 wt.% to 0 wt.%. Regarding these distinct behaviors in regime I and regime II, we postulate that in regime I a high P(NDI2OD-T2) surface content can be maintained as the underlying layer can sustain the overall reduction in P(NDI2OD-T2) content. However, in regime II for which P(NDI2OD-T2) is less than 12.5 wt.%, the P(NDI2OD-T2) content in the remainder of the film drops below the miscibility limit, and a P(NDI2OD-T2) enriched surface content can no longer be maintained. Although displaying a strong tendency of distributing at the free surface, there must be P(NDI2OD-T2) at the substrate/blend film interface as injection of electrons from the Au electrodes at the bottom of the film to the top of the film must be facilitated for OFET operation, which can be experimentally examined by measuring bottom-gate top-contact (BGTC) or bottom-gate bottom-contact (BGBC) devices with the same blend system. In practice, BGTC devices were fabricated with the semiconducting layer containing 75 wt.%, 50 wt.% and 25 wt.% P(NDI2OD-T2), all of which exhibit noticeable field-effect characteristics, confirming the presence of P(NDI2OD-T2) at the bottom interface (see Figure S8 and Table S1 for typical transfer and output curves of those BGBC devices and their performance parameters). In this sense, a schematic

illustration can be helpful to describe the vertical phase separation in those blend films as seen in Figure 5b. No discernable P(NDI2OD-T2) surface content could be determined when the overall P(NDI2OD-T2) content dropped to 1.25 wt.% for TEY mode and 0.25 wt.% for PEY mode. (Note that we have verified that the bulk composition matches that expected based on the solution blend ratio by performing quantitative fitting of blend UV-Vis spectra with neat spectra taken of films of known thickness, see Figure S9, S10 in the Supporting Information. The results confirm that the bulk composition is very close to that expected, and that enrichment of P(NDI2OD-T2) measured at the surface is indeed reflective of surface enrichment rather than a loss of PS from the entire film.)

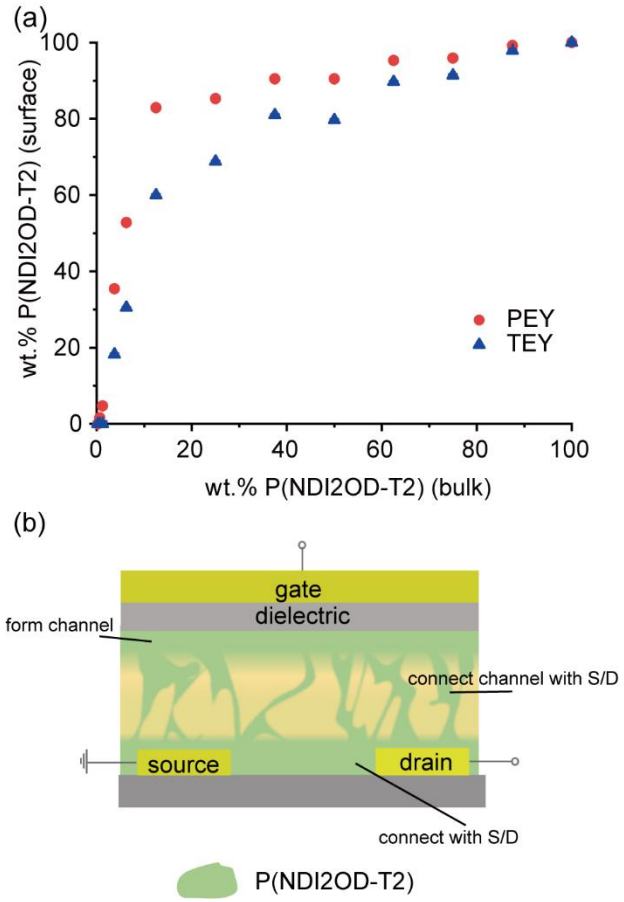

Figure 5. (a) Film composition at the free surface determined by NEXAFS spectroscopy for both PEY and TEY modes with respect to the bulk composition as determined by the blend ratio. (b) Schematic illustration of vertical phase separation within P(NDI2OD-T2)/PS blend films. S/D refers to source/drain electrodes.

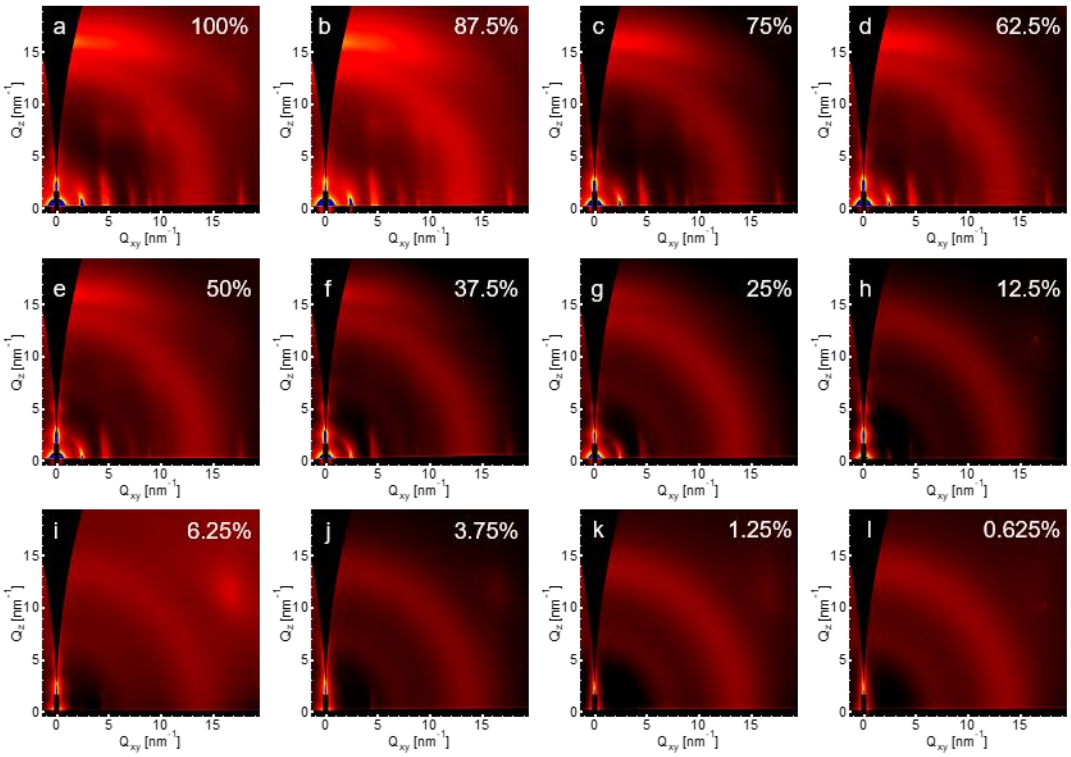

Figure 6. 2D GIWAXS patterns collected at critical angle for films consisting of different content of P(NDI2OD-T2) as indicated on the top right corner. Data shown corresponds to an angle of incidence of ~ 0.1° close to the critical angle at which scattering intensity was maximized.

Crystalline properties. P(NDI2OD-T2) is known to be semicrystalline with a predominately face-on or edge-on orientation depending on the processing conditions.[28] To examine how PS impacts the crystallization behavior of P(NDI2OD-T2) in those blend films, GIWAXS measurements were performed. Figure 6 presents 2D GIWAXS patterns of films with different P(NDI2OD-T2) fractions recorded at critical angles; the corresponding 1D linecuts are displayed in Figure 7. Multiple peaks are observed in the pristine P(NDI2OD-T2) film (Figure 6a and Figure 7), denoting a highly ordered structure. In detail, in the plane of the film, multiple orders (up to four) of *h*00 lamellar stacking peaks (q_{xy} = 0.25 Å^{-1} for the 100 peak) are seen as indexed in the 1D profile in Figure 7, together with a 001 backbone stacking peak (q_{xy} = 0.45 Å^{-1}). The two peaks at q_{xy} = 0.9 Å^{-1} and q_{xy} = 1.8 Å^{-1} are also associated with backbone stacking order, indexed either as the 001′ (q_{xy} = 0.9 Å^{-1}) or 002′ (q_{xy} = 1.8 Å^{-1}) peaks of a second polymorph as inferred by Rivnay et al.,[51] or simply as the 002 and 004 peaks as done

by Trefz et al.[3] In the out-of-plane direction, lamellar stacking peaks 100 (q_z = 0.25 Å^{-1}) and 200 (q_z = 0.49 Å^{-1}), and π-π stacking peak 010 (q_z = 1.6 Å^{-1}) are visible although the lamellar stacking peaks are much weaker than those observed along the in-plane direction. These observations point to a dominant face-on orientation of crystallites with a minority edge-on population, in agreement with prior reports.[5, 7, 26, 27, 51] In contrast to P(NDI2OD-T2), the pure PS film shows only a wide halo at around q = 1.4 Å^{-1} (see Figure S11) due to its amorphous nature.

For blend films with 37.5 wt.% – 100 wt.% P(NDI2OD-T2) the presence of PS barely affects the crystalline properties of P(NDI2OD-T2), with the scattering patterns remaining essentially the same but with a reduction in peak intensity due to the dilution of P(NDI2O-T2). For films with <37.5 wt.% P(NDI2OD-T2), peaks associated with face-on packing appear to reduce in intensity more strongly than those associated with edge-on packing. In particular, the *h00* peaks along the out-of-plane direction appear more prominent and higher orders of *h00* are visible in blend films with decreased P(NDI2OD-T2) content (Figure 6c – Figure 6i). For the neat film (100 wt.% P(NDI2OD-T2)) and blend film with 87.5 wt.% P(NDI2OD-T2) only two orders of *h00* can be discerned (Figure 6a, b). These observations imply a resilience of the edge-on population to reduced P(NDI2OD-T2) content. In the following, we discuss why the nature of the transition from face-on dominated packing to edge-on dominated with decreasing P(NDI2OD-T2) content.

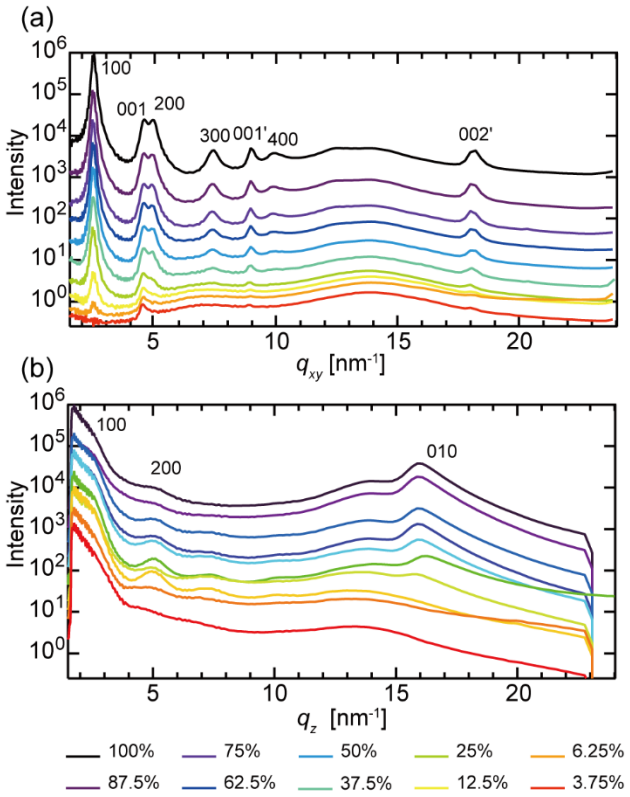

Figure 7. 1D linecuts for in-plane (a) and out-of-plane (b) directions reduced from 2D GIWAXS patterns in Figure 6. Curves are offset for clarity.

Using surface-sensitive NEXAFS spectroscopy, Schuettfort et al. demonstrated that films of P(NDI2OD-T2) have a distinct edge-on orientation at the surface as opposed to face-on orientation in the bulk. In the present study, we can confirm a similar orientation distribution by means of angle-dependent GIWAXS analysis. By tuning the incident angle α_i from below to above the critical angle α_c, GIWAXS measurement can provide depth-dependent structural information.[52-54] Herein, we use the peak area of the out-of-plane 200 peak ($A_{200,OP}$) as a measure of the edge-on population and the area of the in-plane 100 peak ($A_{100,IP}$) as a measure of the face-on population. The ratio of $A_{100,IP}$/ $A_{200,OP}$ thus provides a measure of face-on vs. edge-on texture. (Note that the out-of-plane 200 reflection was selected instead of the 100 reflection because specular contamination made the out-of-plane 100 reflection inaccessible.) As shown in Figure 8a, the ratio $A_{100,IP}/A_{200,OP}$ rises with increasing α_i, indicating relatively enhanced edge-on population at the air/film interface relative to the bulk, consistent with previous studies by

Schuettfort et al.[29] (Note that the trend is not expected to be smooth as there can be strong oscillations in $A_{100,IP}/A_{200,OP}$ due to interference effects.[54]) Additionally, we also observed higher orders of *h00* along the out-of-plane direction and a 010 peak along the in-plane direction in the 2D GIWAXS pattern captured below the critical angle (e.g. at an angle α_i = 0.07°, see Figure S13). These additional peaks which are associated with edge-on packing disappear or are obscured when approaching the critical angle of 0.10° (see Figure S13), once again indicating that edge-on orientation chains are predominantly at the air/film interface.

Regarding blend films with > 6.25 wt.% P(NDI2OD-T2), Figure 8b plots the ratio of $A_{100,IP}/A_{200,OP}$ vs. wt.% P(NDI2OD-T2) at the critical angle. The systematic decrease in the ratio $A_{100,IP}/A_{200,OP}$ with decreasing P(NDI2OD-T2) content provides strong support for an increased proportion of scattering from edge-on lamellae relative to face-on lamellae. The similarity between $A_{100,IP}/A_{200,OP}$ vs. wt.% P(NDI2OD-T2) (Figure 8b) and $A_{100,IP}/A_{200,OP}$ vs. incident angle for neat P(NDI2OD-T2) film (Figure 8a) leads us to consider that the relatively increased scattering from edge-on lamellae in low-P(NDI2OD-T2) films is not because of the presence of PS changing its crystallization properties making edge-on configuration the preferred one, but a result of the reduced P(NDI2OD-T2) content in those blend films. In detail, due to the propensity of P(NDI2OD-T2) of being edge-on at the surface, face-on lamellae in the bulk are reduced relative to edge-on lamellae at the surface with decreasing overall P(NDI2OD-T2) fraction, causing an enhanced edge-on to face-on population in low-P(NDI2OD-T2) films. When P(NDI2OD-T2) content is as low as 6.25 wt.%, both in-plane 100 and out-of-plane 200 peaks could not be fitted confidently.

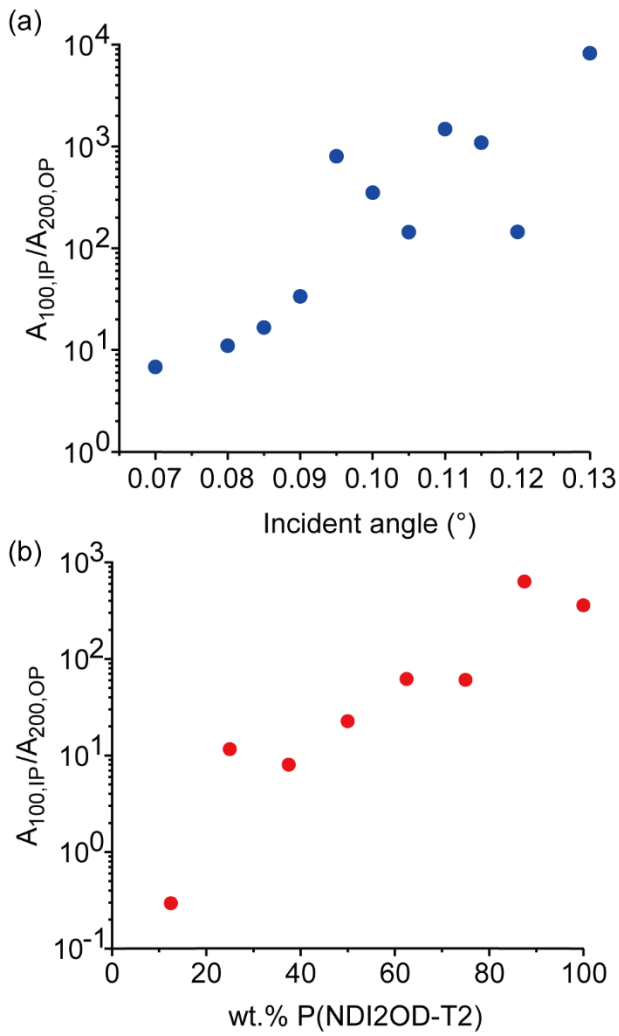

Figure 8. The ratio of peak area of in-plane 100 to out-of-plane 200 ($A_{100,IP}/A_{200,OP}$) as a function of incident angle for neat P(NDI2OD-T2) film (a), and as a function of P(NDI2OD-T2) content (b).

The GIWAXS data was further analyzed by peak fitting to determine parameters of *d*-spacing and crystal coherence length (CCL) based on in-plane lamellar stacking, out-of-plane π-π stacking and in-plane backbone stacking, i.e. 100, 010 and 001. Fitting details are provided in Table S1 along with an example fit shown in Figure S12. From the peak location and FWHM (full width at half maximum), *d*-spacing and CCL were calculated respectively according to $d = \frac{2\pi}{q}$ and Scherrer's equation $\text{CCL} = \frac{2\pi}{FWHM}$. (Note: according to Scherrer's equation, a factor related to crystallite shape is involved, which is not considered in the present study since absolute size is not the main concern in this work.) Values of *d*-spacings and CCLs for neat P(NDI2OD-T2) and blend films are listed in Table S2. To compare changes

in these parameters relative to those of the neat P(NDI2OD-T2) film, ratios of d/d_0 and CCL/CCL_0 were calculated where d_0 and CCL_0 are the *d*-spacing and CCL of neat P(NDI2OD-T2) respectively. These ratios are plotted as a function of P(NDI2OD-T2) content in Figure S14. The effect of PS content on *d*-spacing is minimal for all packing directions with variations of less than 1%. The unchanged lattice *d*-spacings imply that the presence of PS does not affect the packing of P(NDI2OD-T2) on the molecular level. Significant changes are seen, however, in the coherence length. The CCL along the π-π stacking direction (CCL_{010}) gradually decreases by 40% with P(NDI2OD-T2) content decreasing to 25 wt.%; below 25 wt.% a reliable fit could not be obtained. This observation is consistent with the previous study by Wang et al. where they also observed the absence of any 010 reflections in blend films in which P(NDI2OD-T2) was highly diluted.[35] In contrast, the CCL along the backbone direction CCL_{001} is virtually unchanged. Variation of CCL along the 100 direction (CCL_{100}) is minimal until 50 wt.% P(NDI2OD-T2) below which it drops by 40% before the 100 peak disappears. Thus while the presence of PS does not affect how P(NDI2OD-T2) chains pack, it does limit the size of crystallites/degree of order along the π-π stacking and lamellar stacking directions at low P(NDI2OD-T2) content.

Based on the observations provided by the different characterization techniques, the following overall picture is formed: The UV-Vis absorption data implies that P(NDI2OD-T2) chains still strongly aggregate even down to 3.75 wt.% suggesting segregation between PS and P(NDI2OD-T2) chains. AFM and STXM measurements revealed the presence of lateral phase separation between P(NDI2OD-T2) and PS, with the surface of PS-rich phases appearing smooth but with the surface of P(NDI2OD-T2) rich phases having a fibrillary morphology. NEXAFS spectroscopy found evidence for strong vertical phase separation with a P(NDI2OD-T2) surface content of > 80 wt.% maintained down to an overall P(NDI2OD-T2) content of 12.5 wt.%. Taking the AFM and NEXAFS results together implies that the smooth surface of the PS-rich domain is still covered by a skin layer of P(NDI2OD-T2). While the GIWAXS results showed a dominant face-on orientation in the bulk, a minority edge-on population at

the surface was inferred from angle-dependent measurements. The edge-on population was found to be resilient to decreasing P(NDI2OD-T2), becoming the dominant population at very low P(NDI2OD-T2) content. The coincidence of the disappearance of the out-of-plane 010 peak in GIWAXS and fibrils in the AFM at 12.5 wt.% also suggests that these fibrils are associated with face-on crystallites having structural order along the three crystallographic directions.

Electrical properties based on OFETs. To evaluate the electrical properties of P(NDI2OD-T2)/PS blends, TGBC OFET devices based on blend films with varying P(NDI2OD-T2) content were fabricated and measured. Figure 9a shows the variation of mobility as a function of P(NDI2OD-T2) content in P(NDI2OD-T2)/PS blend films (output characteristics and transfer curves are provided in the supporting information). Overall, the trend shown here is reminiscent of those reported by Qiu et al. and Goffri et al. for the P3HT/PS blend system.[17, 19] The plot of mobility vs. P(NDI2OD-T2) content can be divided into two regions: in the range of 25 wt.% to 100 wt.% the mobility drops gradually from 0.4 $cm^2/(V{\cdot}s)$ to 0.1 $cm^2/(V{\cdot}s)$, while between 12.5 wt.% to 0.625 wt.% the mobility drops dramatically from 0.03 $cm^2/(V{\cdot}s)$ to 0.001 $cm^2/(V{\cdot}s)$. This dramatic drop in mobility is accompanied by growing hysteresis in the *I–V* curves (see Figure S15). Though displaying poor-quality *I–V* curves, a clear field effect can still be observed for devices with only 0.625 wt.% P(NDI2OD-T2) (Figure S15). Below 0.625 % P(NDI2OD-T2), no OFET performance is observed, presumably due to the disruption of charge transport pathways in highly diluted P(NDI2OD-T2) films. Examining the threshold voltage, it is found to remain constant in the range of 20 wt.% to 100 wt.%; below 20 wt.% it rapidly increases with decreasing P(NDI2OD-T2) (Figure 9b). For comparison, the performance of devices made from neat P(NDI2OD-T2) films with the same concentration of P(NDI2OD-T2) but no PS content are overlaid in Figure 9. Irrespective of the incorporation of PS, both mobility and threshold voltage show similar trends in neat and blend films, though the mobility is seen to remain slightly higher for neat P(NDI2OD-T2) films and the threshold voltage increases at a lower concentration of P(NDI2OD-T2), demonstrating the advantage of this blending method in reducing the consumption of expensive semiconducting materials at no cost to

electrical properties. Additionally, we also noticed growing hysteresis and device-to-device variation in both mobility and threshold voltage with decreasing P(NDI2OD-T2) content, as can be seen in Figure 9 and Figure S15.

When measuring the device mobility in the saturation regime according to equation (1), channel length and width are set to be 20 μm and 10 mm respectively, as defined by the device geometry. This holds only when the conductive channel near the film/air interface in our TGBC devices is completely made up of semiconductor materials. Yet, it is evident the channel is not fully covered by P(NDI2OD-T2), causing the effective channel width to deviate from that defined by the device geometry. Thus, mobilities were corrected according to equation (1) on the basis of saturation mobility μ being inversely proportional to the channel width W, with more details shown in Figure S16. Overall, a negligible difference is seen between corrected and uncorrected OFET mobilities.

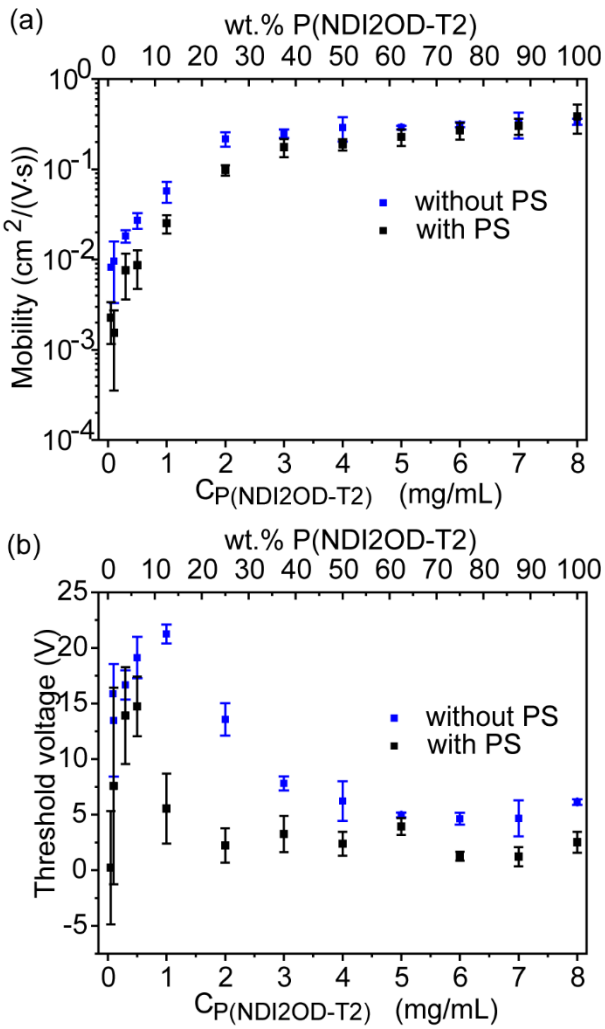

Figure 9. Mobility (a) and threshold voltage (b) as a function of P(NDI2OD-T2) fraction (black), and as a function of the solution concentration of P(NDI2OD-T2) for neat films (blue). Error bars reflect variations in device performance observed across multiple devices; most error bars are based on an average of 6 – 8 devices with concentrations of 1.25 wt.% (0.1 mg/mL) and 0.625 wt.% (0.05 mg/mL) being based on 3 – 4 devices.

Structure/property relationship. We ultimately aim to link the electrical performance of OFET devices to the morphological properties extracted from the various characterizations of the active layer. The observed mobility trends appear to correlate well with the trends observed by NEXAFS spectroscopy. Both mobility and P(NDI2OD-T2) surface content show a similar trend with respect to overall P(NDI2OD-T2) content with similar turning points in the range of 12.5 wt.% – 25 wt.% (Figure 10). In

addition, both show a similar percolation threshold of 0.625 wt.% below which no current was measured in OFETs and no P(NDI2OD-T2) surface content discernible with PEY NEXAFS spectroscopy. Between the ranges of 25 wt.% and 100 wt.% it is remarkable that the presence of lateral phase separation appears to have little influence on the device properties, with Wang et al. previously linking the presence of lateral phase separation with a lack of OFET function.[35] These observations lead us to postulate that device mobility primarily depends on the film composition at the semiconductor/dielectric interface, i.e., the top surface of blend films in TGBC devices. In detail, device performance or charge transport is highly dependent on the formation of continuous percolation pathways for charges to move through. The existence of continuous pathways at the semiconductor/dielectric interface will depend primarily on surface composition, with the overall composition of 25 wt.% appearing to be a critical composition above which percolation pathways are well-formed, but below which the connectivity of pathways drastically deteriorates, consistent with the rapidly reduced P(NDI2OD-T2) content in the film surface indicated by PEY NEXAFS spectroscopy. The percolative behaviors of OFET mobility were also observed in many other blend systems.[19, 21, 55]

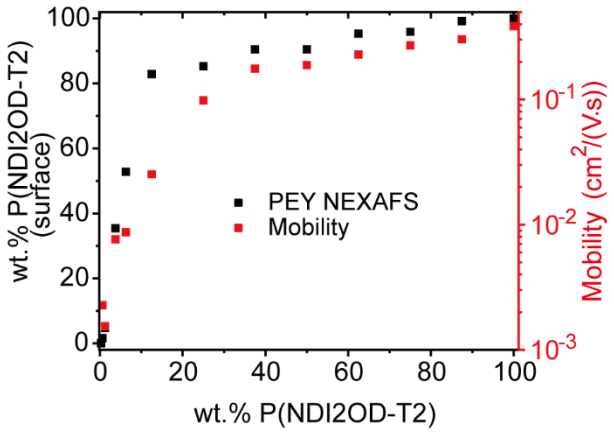

Figure 10. Film composition probed at the film surface and corresponding device mobility as a function of P(NDI2OD-T2) content in the blend films.

The strong correlation between surface composition and OFET performance does not mean that the bulk microstructure is not playing a supporting role. While intrachain transport is recognized to be more

efficient than interchain transport (mainly along the π-π stacking direction), charges would often need to transport via interchain hopping in order to avoid transport bottlenecks. Besides, improved charge carrier mobilities via three-dimensional transport in films with a bimodal orientation of face-on and edge-on have been reported in previous studies.[56-61] In the case of P(NDI2OD-T2), ordered packing along the π-π stacking direction is mainly limited to face-on crystallites in the bulk. Based on earlier discussion, both the face-on population (**Figure 8**b) and the coherence length along the π-π stacking direction (Figure S14) are suppressed with reducing P(NDI2OD-T2) content, which we believe may be responsible for the slightly inferior performance of those blend devices to their neat counterparts (see **Figure 9**a). That is, dilution of P(NDI2OD-T2) by PS in the bulk may by negatively affecting three-dimensional transport and interchain hopping. As to the variation of mobility of neat P(NDI2OD-T2), it is less sensitive to the concentration of the casting solution until 1 g/L, below which a uniform film of P(NDI2OD-T2) cannot be sustained leading ultimately to a loss in P(NDI2OD-T2) connectivity (see Figure S17 for AFM images), agreeing with previous studies.[23, 24]

Taken together, we propose the following structure/property relationship. Owing to its lower surface free energy compared to PS, P(NDI2OD-T2) has a strong propensity to segregate at the air/film interface. In the range of 25 wt.% – 100 wt.%, the surfaces of these blend films are mainly covered with > 80 wt.% P(NDI2OD-T2). A high P(NDI2OD-T2) content together with lateral phase separation from PS allows P(NDI2OD-T2) chains to crystallize in the bulk with a face-on orientation. In this case, the well-identified π-π stacking order along the out-of-plane direction allows a three-dimensional transport mode that was found to be beneficial to high charge carrier mobility compared to two-dimensional transport in unimodal films.[56-61] Additionally, the presence of face-on oriented chains in phase-segregated P(NDI2OD-T2)-rich domains assists in ensuring well-connected pathways across the film connecting the source and drain electrodes to the top charge transporting interface. In the range of < 25 wt.%, lateral phase separation and signatures of face-on bulk crystallites disappear. These observations indicate that

P(NDI2OD-T2) chains are likely to be disordered in the bulk and at a concentration below the miscibility limit of P(NDI2OD-T2) in PS. This change in bulk properties negatively impacts upon 3D charge transport within and near the charge accumulation layer and may disrupt charge transport from the source and drain electrodes to the top surface. Ultimately with decreasing P(NDI2OD-T2) loading, the amount of P(NDI2OD-T2) segregated at the semiconductor/dielectric interface drops below a value that can sustain charge transport.

Finally, it is worth noting differences between P(NDI2OD-T2)/PS blends and P3HT/PS blends. Though displaying similar trends of mobility as a function of film composition, P(NDI2OD-T2)/PS and P3HT/PS exhibit distinct morphology evolutions.[21, 49] In the P3HT/PS system, P3HT tends to forms one-dimensional fibers with a high aspect ratio depending on the processing solvent, indicative of long-range ordering. These fibers are then easily able to interconnect with each other, forming a continuous P3HT network that is crucial to sustain efficient charge transport in blends with PS. Since the formation of P3HT fibers is not strongly affected by the addition of PS, the mobility of P3HT/PS blend films is comparable to that of neat P3HT films until a rather low concentration of P3HT. In contrast, the long range ordering of P(NDI2OD-T2) is degraded with reducing P(NDI2OD-T2) content. Nevertheless, such a degradation has a limited impact on the charge transport properties of P(NDI2OD-T2). Different morphology dependence of mobility between P3HT/PS and P(NDI2OD-T2)/PS can be explained in terms of the difference between the properties of P3HT and P(NDI2OD-T2). P3HT is known as one of the first-generation or "classic" conjugated polymers, from which a paradigm was established that a high degree of order or crystallinity was necessary for high charge carrier mobility. This concept later was challenged by second-generation conjugated polymers represented by P(NDI2OD-T2), which have shown performance comparable to or even better than that of first-generation polymers but with reduced long range order.[62] Second generation polymers have been found to have improved local order due to their more planar backbones, which render their macroscopic electronic properties more resilient to long-ranged disorder, commonly seen in semicrystalline polymers. Interestingly in a recent study researchers

fabricated OFET devices based on three-dimensional bulk semiconductor structures with persistent molecular arrangement throughout the thickness using channel-die pressing, which allowed them to evaluate charge transport properties along all three crystallographic axes, i.e., backbone, π-π stacking and lamellar stacking directions.[63] It was found that the highest mobility was achieved along the π-π stacking direction for P3HT, as opposed to backbone direction for P(NDI2OD-T2), reaffirming different properties of long-range order in P3HT and short-ranged order in P(NDI2OD-T2). Note that although short-range order is sufficient to sustain efficient charge transport in P(NDI2OD-T2), this does not mean that improving long-range order along π-π stacking direction would not promote it performance further.

Conclusion

In conclusion, we have systematically investigated the electrical and morphological properties of P(NDI2OD-T2)/PS blends across a large compositional range. UV–Vis absorption spectroscopy measurements found that the nature of chain aggregation was largely unaffected by blending. AFM and STXM measurements provided evidence for lateral phase segregation for P(NDI2OD-T2) compositions of 87.5 wt.% to 25 wt.% P(NDI2OD-T2), with a P(NDI2OD-T2)-rich surface layer that persists down to 12.5 wt.% P(NDI2OD-T2) as revealed by NEXAFS measurements. GIWAXS measurements found a negligible change in the lattice spacing in three crystallographic directions. Variations in the crystal coherence lengths however were observed, with the coherence length of different crystallographic directions showing distinct dependencies on blend ratio. With reducing P(NDI2OD-T2) content, an increase in the relative fraction of edge-on lamellae compared to face-on lamellae was found. By comparing the various microstructural and morphological changes with the observed change in OFET performance as a function of P(NDI2OD-T2) content, a composition/structure/property relationship was proposed, with surface connectivity found to be the most important parameter and lateral phase separation having a surprisingly weak effect. This research provides guidance for morphology

optimization in conjugated polymer/insulating polymer blends which will be relevant for future studies seeking to optimize mechanical and electrical properties for wearable electronics.

ASSOCIATED CONTENT

Supporting information

The supporting information is available free of charge.

STXM parameters, normalized optical absorption spectra, atomic force microscopy and scanning transmission X-ray microscopy images, details of NEXAFS fitting, BGTC OFET data, bulk composition determined from UV-Vis-NIR measurements, 2D GIWAXS pattern of neat PS, multi-peak fitting parameters and extracted lattice parameters, GIWAXS data below critical angle, output and transfer curves for OFETs, mobility correction (PDF), AFM images of neat P(DNI2OD-T2) as a function of solution concentration.

AUTHOR INFORMATION

Corresponding Author

*E-mail christopher.mcneill@monash.edu.

Notes

The authors declare no competing financial interests.

ACKNOWLEDGMENT

L.T. thanks Dr. Wen Liang Tan for discussion on GIWAXS data processing. This work was performed in part at the Soft X-ray and SAXS/WAXS beamlines at the Australian Synchrotron, part of ANSTO. The PolLux end station was financed by the German Ministerium für Bildung und Forschung (BMBF) through contracts 05K16WED and 05K19WE2. This work was also performed in part at the Melbourne

Centre for Nanofabrication (MCN) in the Victorian Node of the Australian National Fabrication Facility (ANFF).

REFERENCES

(1) Forrest, S. R. The path to ubiquitous and low-cost organic electronic appliances on plastic. *Nature* **2004,** 428 (6986), 911-918.

(2) Yan, H.; Chen, Z.; Zheng, Y.; Newman, C.; Quinn, J. R.; Dötz, F.; Kastler, M.; Facchetti, A. A high-mobility electron-transporting polymer for printed transistors. *Nature* **2009,** 457 (7230), 679-686.

(3) Trefz, D.; Gross, Y. M.; Dingler, C.; Tkachov, R.; Hamidi-Sakr, A.; Kiriy, A.; McNeill, C. R.; Brinkmann, M.; Ludwigs, S. Tuning Orientational Order of Highly Aggregating P(NDI2OD-T2) by Solvent Vapor Annealing and Blade Coating. *Macromolecules* **2019,** 52 (1), 43-54.

(4) Tremel, K.; Fischer, F. S. U.; Kayunkid, N.; Pietro, R. D.; Tkachov, R.; Kiriy, A.; Neher, D.; Ludwigs, S.; Brinkmann, M. Charge Transport Anisotropy in Highly Oriented Thin Films of the Acceptor Polymer P(NDI2OD-T2). *Advanced Energy Materials* **2014,** 4 (10), 1301659.

(5) Nahid, M. M.; Matsidik, R.; Welford, A.; Gann, E.; Thomsen, L.; Sommer, M.; McNeill, C. R. Unconventional Molecular Weight Dependence of Charge Transport in the High Mobility n-type Semiconducting Polymer P(NDI2OD-T2). *Adv. Funct. Mater.* **2017,** 27 (9), 1604744.

(6) Steyrleuthner, R.; Di Pietro, R.; Collins, B. A.; Polzer, F.; Himmelberger, S.; Schubert, M.; Chen, Z.; Zhang, S.; Salleo, A.; Ade, H.; Facchetti, A.; Neher, D. The Role of Regioregularity, Crystallinity, and Chain Orientation on Electron Transport in a High-Mobility n-Type Copolymer. *J. Am. Chem. Soc.* **2014,** 136 (11), 4245-4256.

(7) Schuettfort, T.; Huettner, S.; Lilliu, S.; Macdonald, J. E.; Thomsen, L.; McNeill, C. R. Surface and Bulk Structural Characterization of a High-Mobility Electron-Transporting Polymer. *Macromolecules* **2011,** 44 (6), 1530-1539.

(8) Chen, Z.; Zheng, Y.; Yan, H.; Facchetti, A. Naphthalenedicarboximide- vs Perylenedicarboximide-Based Copolymers. Synthesis and Semiconducting Properties in Bottom-Gate N-Channel Organic Transistors. *J. Am. Chem. Soc.* **2009,** 131 (1), 8-9.

(9) Wang, G.; Persson, N.; Chu, P.-H.; Kleinhenz, N.; Fu, B.; Chang, M.; Deb, N.; Mao, Y.; Wang, H.; Grover, M. A.; Reichmanis, E. Microfluidic Crystal Engineering of π-Conjugated Polymers. *ACS Nano* **2015,** 9 (8), 8220-8230.

(10) Kline, R. J.; McGehee, M. D.; Kadnikova, E. N.; Liu, J.; Fréchet, J. M. J.; Toney, M. F. Dependence of Regioregular Poly(3-hexylthiophene) Film Morphology and Field-Effect Mobility on Molecular Weight. *Macromolecules* **2005,** 38 (8), 3312-3319.

(11) Persson, N. E.; Chu, P.-H.; McBride, M.; Grover, M.; Reichmanis, E. Nucleation, Growth, and Alignment of Poly(3-hexylthiophene) Nanofibers for High-Performance OFETs. *Acc. Chem. Res.* **2017,** 50 (4), 932-942.

(12) Zhang, G.; McBride, M.; Persson, N.; Lee, S.; Dunn, T. J.; Toney, M. F.; Yuan, Z.; Kwon, Y.-H.; Chu, P.-H.; Risteen, B.; Reichmanis, E. Versatile Interpenetrating Polymer Network Approach to Robust Stretchable Electronic Devices. *Chem. Mater.* **2017,** 29 (18), 7645-7652.

(13) Zhang, G.; Lee, S.; Gutiérrez-Meza, E.; Buckley, C.; McBride, M.; Valverde-Chávez, D. A.; Kwon, Y. H.; Savikhin, V.; Xiong, H.; Dunn, T. J.; Toney, M. F.; Yuan, Z.; Silva, C.; Reichmanis, E. Robust and Stretchable Polymer Semiconducting Networks: From Film Microstructure to Macroscopic Device Performance. *Chem. Mater.* **2019,** 31 (17), 6530-6539.

(14) Wang, X.; Lee, W. H.; Zhang, G.; Wang, X.; Kang, B.; Lu, H.; Qiu, L.; Cho, K. Self-stratified semiconductor/dielectric polymer blends: vertical phase separation for facile fabrication of organic transistors. *J. Mater. Chem. C* **2013,** 1 (25), 3989-3998.

(15) Rinehart, S. J.; Yuan, G.; Dadmun, M. D. The interplay of thermodynamics and kinetics: imparting hierarchical control over film formation of self-stratified blends. *Soft Matter* **2020,** 16 (5), 1287-1297.

(16) Rinehart, S. J.; Yuan, G.; Dadmun, M. D. Elucidating the Kinetic and Thermodynamic Driving Forces in Polymer Blend Film Self-Stratification. *Macromolecules* **2018,** 51 (19), 7836-7844.

(17) Qiu, L.; Lim, J. A.; Wang, X.; Lee, W. H.; Hwang, M.; Cho, K. Versatile Use of Vertical-Phase-Separation-Induced Bilayer Structures in Organic Thin-Film Transistors. *Adv. Mater.* **2008,** 20 (6), 1141-1145.

(18) Hou, S.; Yu, J.; Zhuang, X.; Li, D.; Liu, Y.; Gao, Z.; Sun, T.; Wang, F.; Yu, X. Phase Separation of P3HT/PMMA Blend Film for Forming Semiconducting and Dielectric Layers in Organic Thin-Film Transistors for High-Sensitivity NO2 Detection. *ACS Appl. Mater. Interfaces* **2019,** 11 (47), 44521-44527.

(19) Goffri, S.; Müller, C.; Stingelin-Stutzmann, N.; Breiby, D. W.; Radano, C. P.; Andreasen, J. W.; Thompson, R.; Janssen, R. A. J.; Nielsen, M. M.; Smith, P.; Sirringhaus, H. Multicomponent semiconducting polymer systems with low crystallization-induced percolation threshold. *Nat. Mater.* **2006,** 5 (12), 950-956.

(20) Arias, A. C.; Endicott, F.; Street, R. A. Surface-Induced Self-Encapsulation of Polymer Thin-Film Transistors. *Adv. Mater.* **2006,** 18 (21), 2900-2904.

(21) Qiu, L.; Lee, W. H.; Wang, X.; Kim, J. S.; Lim, J. A.; Kwak, D.; Lee, S.; Cho, K. Organic Thin-film Transistors Based on Polythiophene Nanowires Embedded in Insulating Polymer. *Adv. Mater.* **2009,** 21 (13), 1349-1353.

(22) Brinkmann, M.; Gonthier, E.; Bogen, S.; Tremel, K.; Ludwigs, S.; Hufnagel, M.; Sommer, M. Segregated versus Mixed Interchain Stacking in Highly Oriented Films of Naphthalene Diimide Bithiophene Copolymers. *ACS Nano* **2012,** 6 (11), 10319-10326.

(23) Bucella, S. G.; Luzio, A.; Gann, E.; Thomsen, L.; McNeill, C. R.; Pace, G.; Perinot, A.; Chen, Z.; Facchetti, A.; Caironi, M. Macroscopic and high-throughput printing of aligned nanostructured polymer semiconductors for MHz large-area electronics. *Nat. Commun.* **2015,** 6 (1), 8394.

(24) Karpov, Y.; Zhao, W.; Raguzin, I.; Beryozkina, T.; Bakulev, V.; Al-Hussein, M.; Häußler, L.; Stamm, M.; Voit, B.; Facchetti, A.; Tkachov, R.; Kiriy, A. Influence of Semiconductor Thickness and Molecular Weight on the Charge Transport of a Naphthalenediimide-Based Copolymer in Thin-Film Transistors. *ACS Appl. Mater. Interfaces* **2015,** 7 (23), 12478-12487.

(25) Luzio, A.; Criante, L.; D'Innocenzo, V.; Caironi, M. Control of charge transport in a semiconducting copolymer by solvent-induced long-range order. *Sci. Rep.* **2013,** 3 (1), 3425.

(26) Meyer, D. L.; Matsidik, R.; Huettner, S.; Sommer, M.; Biskup, T. Solvent-mediated aggregate formation of PNDIT2: decreasing the available conformational subspace by introducing locally highly ordered domains. *Phys. Chem. Chem. Phys.* **2018,** 20 (4), 2716-2723.

(27) Nahid, M. M.; Welford, A.; Gann, E.; Thomsen, L.; Sharma, K. P.; McNeill, C. R. Nature and Extent of Solution Aggregation Determines the Performance of P(NDI2OD-T2) Thin-Film Transistors. *Adv. Electron. Mater.* **2018,** 4 (4), 1700559.

(28) Rivnay, J.; Steyrleuthner, R.; Jimison, L. H.; Casadei, A.; Chen, Z.; Toney, M. F.; Facchetti, A.; Neher, D.; Salleo, A. Drastic Control of Texture in a High Performance n-Type Polymeric Semiconductor and Implications for Charge Transport. *Macromolecules* **2011,** 44 (13), 5246-5255.

(29) Schuettfort, T.; Thomsen, L.; McNeill, C. R. Observation of a Distinct Surface Molecular Orientation in Films of a High Mobility Conjugated Polymer. *J. Am. Chem. Soc.* **2013,** 135 (3), 1092-1101.

(30) Steyrleuthner, R.; Schubert, M.; Howard, I.; Klaumünzer, B.; Schilling, K.; Chen, Z.; Saalfrank, P.; Laquai, F.; Facchetti, A.; Neher, D. Aggregation in a High-Mobility n-Type Low-Bandgap Copolymer with Implications on Semicrystalline Morphology. *J. Am. Chem. Soc.* **2012,** 134 (44), 18303-18317.

(31) Jiang, Y.; Ning, L.; Liu, C.; Sun, Y.; Li, J.; Liu, Z.; Yi, Y.; Qiu, D.; He, C.; Guo, Y.; Hu, W.; Liu, Y. Alignment of linear polymeric grains for highly stable N-type thin-film transistors. *Chem* **2021,** 7 (5), 1258-1270.

(32) Persson, N. E.; Engmann, S.; Richter, L. J.; DeLongchamp, D. M. In Situ Observation of Alignment Templating by Seed Crystals in Highly Anisotropic Polymer Transistors. *Chem. Mater.* **2019,** 31 (11), 4133-4147.

(33) Angunawela, I.; Nahid, M. M.; Ghasemi, M.; Amassian, A.; Ade, H.; Gadisa, A. The Critical Role of Materials' Interaction in Realizing Organic Field-Effect Transistors Via High-Dilution Blending with Insulating Polymers. *ACS Appl. Mater. Interfaces* **2020,** 12 (23), 26239-26249.

(34) Yang, H.-R.; Pai, C.-W.; Sun, H.-S.; Wu, C.; Lai, Y.-Y.; Haw, S.-C.; Lee, J.-J.; Chen, J.-M. Establishment of the Interconnectivity among P (NDI2OD-T2) s in Organic Field-Effect Transistors by Non-Conjugated Crystalline Polymers. *Macromolecules* **2020,** 53 (23), 10349-10356.

(35) Wang, S.; Fabiano, S.; Himmelberger, S.; Puzinas, S.; Crispin, X.; Salleo, A.; Berggren, M. Experimental evidence that short-range intermolecular aggregation is sufficient for efficient charge transport in conjugated polymers. *Proc. Natl. Acad. Sci.* **2015,** 112 (34), 10599.

(36) Dong, J.; Wang, Y.; Mori, T.; Michinobu, T. Improving the air-stability of n-type organic thin-film transistors by polyacrylonitrile additive. *Jpn. J. Appl. Phys.* **2019,** 59 (SD), SDDC05.

(37) Zhou, Y.; Fuentes-Hernandez, C.; Shim, J.; Meyer, J.; Giordano, A. J.; Li, H.; Winget, P.; Papadopoulos, T.; Cheun, H.; Kim, J.; Fenoll, M.; Dindar, A.; Haske, W.; Najafabadi, E.; Khan, T. M.; Sojoudi, H.; Barlow, S.; Graham, S.; Brédas, J.-L.; Marder, S. R.; Kahn, A.; Kippelen, B. A Universal Method to Produce Low–Work Function Electrodes for Organic Electronics. *Science* **2012,** 336 (6079), 327.

(38) Raabe, J.; Tzvetkov, G.; Flechsig, U.; Böge, M.; Jaggi, A.; Sarafimov, B.; Vernooij, M. G. C.; Huthwelker, T.; Ade, H.; Kilcoyne, D.; Tyliszczak, T.; Fink, R. H.; Quitmann, C. PolLux: A new facility for soft x-ray spectromicroscopy at the Swiss Light Source. *Rev. Sci. Instrum.* **2008,** 79 (11), 113704.

(39) McNeill, C. R.; Watts, B.; Thomsen, L.; Belcher, W. J.; Greenham, N. C.; Dastoor, P. C. Nanoscale Quantitative Chemical Mapping of Conjugated Polymer Blends. *Nano Lett.* **2006,** 6 (6), 1202-1206.

(40) Kirby, N. M.; Mudie, S. T.; Hawley, A. M.; Cookson, D. J.; Mertens, H. D. T.; Cowieson, N.; Samardzic-Boban, V. A low-background-intensity focusing small-angle X-ray scattering undulator beamline. *J. Appl. Crystallogr.* **2013,** 46 (6), 1670-1680.

(41) Ilavsky, J. Nika: software for two-dimensional data reduction. *J. Appl. Crystallogr.* **2012,** 45 (2), 324-328.

(42) Cowie, B. C. C.; Tadich, A.; Thomsen, L. The Current Performance of the Wide Range (90 – 2500 eV) Soft X - ray Beamline at the Australian Synchrotron. *AIP Conf. Proc.* **2010,** 1234 (1), 307-310.

(43) Wang, W.-C.; Chen, S.-Y.; Yang, Y.-W.; Hsu, C.-S.; Tajima, K. Face-on reorientation of π-conjugated polymers in thin films by surface-segregated monolayers. *J. Mater. Chem. A* **2020,** 8 (13), 6268-6275.

(44) Harris, M.; Appel, G.; Ade, H. Surface Morphology of Annealed Polystyrene and Poly(methyl methacrylate) Thin Film Blends and Bilayers. *Macromolecules* **2003,** 36 (9), 3307-3314.

(45) Chua, L.-L.; Dipankar, M.; Sivaramakrishnan, S.; Gao, X.; Qi, D.; Wee, A. T. S.; Ho, P. K. H. Large Damage Threshold and Small Electron Escape Depth in X-ray Absorption Spectroscopy of a Conjugated Polymer Thin Film. *Langmuir* **2006,** 22 (20), 8587-8594.

(46) Gann, E.; McNeill, C. R.; Tadich, A.; Cowie, B. C. C.; Thomsen, L. Quick AS NEXAFS Tool (QANT): a program for NEXAFS loading and analysis developed at the Australian Synchrotron. *J. Synchrotron Radiat.* **2016,** 23 (1), 374-380.

(47) Nahid, M. M.; Gann, E.; Thomsen, L.; McNeill, C. R. NEXAFS spectroscopy of conjugated polymers. *Eur. Polym. J.* **2016,** 81, 532-554.

(48) Xiong, M.; Yan, X.; Li, J. T.; Zhang, S.; Cao, Z.; Prine, N.; Lu, Y.; Wang, J. Y.; Gu, X.; Lei, T. Efficient n‐Doping of Polymeric Semiconductors through Controlling the Dynamics of Solution‐State Polymer Aggregates. *Angew. Chem.* **2021,** 133 (15), 8270-8278.

(49) Qiu, L.; Wang, X.; Lee, W. H.; Lim, J. A.; Kim, J. S.; Kwak, D.; Cho, K. Organic Thin-Film Transistors Based on Blends of Poly(3-hexylthiophene) and Polystyrene with a Solubility-Induced Low Percolation Threshold. *Chem. Mater.* **2009,** 21 (19), 4380-4386.

(50) Rösner, B.; Koch, F.; Döring, F.; Guzenko, V. A.; Meyer, M.; Ornelas, J. L.; Späth, A.; Fink, R. H.; Stanescu, S.; Swaraj, S.; Belkhou, R.; Watts, B.; Raabe, J.; David, C. 7 nm Spatial Resolution in Soft X-ray Microscopy. *Microsc. Microanal.* **2018,** 24 (S2), 270-271.

(51) Rivnay, J.; Toney, M. F.; Zheng, Y.; Kauvar, I. V.; Chen, Z.; Wagner, V.; Facchetti, A.; Salleo, A. Unconventional Face-On Texture and Exceptional In-Plane Order of a High Mobility n-Type Polymer. *Adv. Mater.* **2010,** 22 (39), 4359-4363.

(52) Widjonarko, N. E. Introduction to Advanced X-ray Diffraction Techniques for Polymeric Thin Films. *Coatings* **2016,** 6 (4), 54.

(53) Renaud, G.; Lazzari, R.; Leroy, F. Probing surface and interface morphology with Grazing Incidence Small Angle X-Ray Scattering. *Surf. Sci. Rep.* **2009,** 64 (8), 255-380.

(54) Gann, E.; Caironi, M.; Noh, Y.-Y.; Kim, Y.-H.; McNeill, C. R. Diffractive X-ray Waveguiding Reveals Orthogonal Crystalline Stratification in Conjugated Polymer Thin Films. *Macromolecules* **2018,** 51 (8), 2979-2987.

(55) Smith, J.; Heeney, M.; McCulloch, I.; Malik, J. N.; Stingelin, N.; Bradley, D. D. C.; Anthopoulos, T. D. Percolation behaviour in high mobility p-channel polymer/small-molecule blend organic field-effect transistors. *Org. Electron.* **2011,** 12 (1), 143-147.

(56) Kim, Y.; Long, D. X.; Lee, J.; Kim, G.; Shin, T. J.; Nam, K.-W.; Noh, Y.-Y.; Yang, C. A Balanced Face-On to Edge-On Texture Ratio in Naphthalene Diimide-Based Polymers with Hybrid Siloxane Chains Directs Highly Efficient Electron Transport. *Macromolecules* **2015,** 48 (15), 5179-5187.

(57) Lee, J.; Han, A. R.; Yu, H.; Shin, T. J.; Yang, C.; Oh, J. H. Boosting the Ambipolar Performance of Solution-Processable Polymer Semiconductors via Hybrid Side-Chain Engineering. *J. Am. Chem. Soc.* **2013,** 135 (25), 9540-9547.

(58) Lim, D.-H.; Kim, Y.-J.; Kim, Y.-A.; Hwang, K.; Park, J.-J.; Kim, D.-Y. Structural Insight into Aggregation and Orientation of TPD-Based Conjugated Polymers for Efficient Charge-Transporting Properties. *Chem. Mater.* **2019,** 31 (13), 4629-4638.

(59) Mei, J.; Kim, D. H.; Ayzner, A. L.; Toney, M. F.; Bao, Z. Siloxane-Terminated Solubilizing Side Chains: Bringing Conjugated Polymer Backbones Closer and Boosting Hole Mobilities in Thin-Film Transistors. *J. Am. Chem. Soc.* **2011,** 133 (50), 20130-20133.

(60) Park, S.; Lee, M. H.; Ahn, K. S.; Choi, H. H.; Shin, J.; Xu, J.; Mei, J.; Cho, K.; Bao, Z.; Lee, D. R.; Kang, M. S.; Kim, D. H. Combinatorial Study of Temperature-Dependent Nanostructure and Electrical Conduction of Polymer Semiconductors: Even Bimodal Orientation Can Enhance 3D Charge Transport. *Adv. Funct. Mater.* **2016,** 26 (26), 4627-4634.

(61) Qiao, X.; Wu, Q.; Wu, H.; Zhang, J.; Li, H. Bithienopyrroledione-Based Copolymers, Versatile Semiconductors for Balanced Ambipolar Thin-Film Transistors and Organic Solar Cells with V oc > 1 V. *Adv. Funct. Mater.* **2017,** 27 (4), 1604286.

(62) Noriega, R.; Rivnay, J.; Vandewal, K.; Koch, F. P.; Stingelin, N.; Smith, P.; Toney, M. F.; Salleo, A. A general relationship between disorder, aggregation and charge transport in conjugated polymers. *Nat. Mater.* **2013,** 12 (11), 1038-1044.

(63) Yu, L.; Pavlica, E.; Li, R.; Zhong, Y.; Silva, C.; Bratina, G.; Müller, C.; Amassian, A.; Stingelin, N. Conjugated polymer mesocrystals with structural and optoelectronic coherence and anisotropy in three dimensions. https://onlinelibrary.wiley.com/doi/abs/10.1002/adma.202103002